Journal of Materials Chemistry C

ROYAL SOCIETY OF CHEMISTRY

PAPER

View Article Online
View Journal | View Issue



Cite this: J. Mater. Chem. C, 2021, 9, 10478

# Silicon-based two-dimensional chalcogenide of p-type semiconducting silicon telluride nanosheets for ultrahigh sensitive photodetector applications†

Chang-Yu Lin, ‡*[a] Rajesh Kumar Ulaganathan, ‡*[bc] Raman Sankar, *[d] Raghavan Chinnambedu Murugesan,[e] Ambika Subramanian,[a] Alex Rozhin[e] and Shaik Firdoz [f]

Two-dimensional (2D) materials have attracted significant attention in recent years owing to their exotic properties. Semiconducting p-type 2D crystals are crucial to the construction of versatile p–n junction-based nanoelectronic devices, and promising future optoelectronic applications. Herein, we reported the growth of high-quality p-type silicon telluride ($Si_2Te_3$) single crystals using the chemical vapor transport (CVT) technique. Few layered $Si_2Te_3$ nanosheets were obtained by mechanical exfoliation and used to fabricate a phototransistor device under a rigid silicon substrate. The $Si_2Te_3$ nanosheet-based transistor exhibits an outstanding device performance, such as a high photoresponsivity of approximately 1396 A $W^{-1}$ and a larger specific detectivity of approximately 2.52 × $10^{12}$ Jones at a wavelength of 633 nm. The values obtained using the $Si_2Te_3$ single crystal are remarkably superior to those obtained for the other chalcogenide 2D crystals, such as $Bi_2Te_3$ and $Sb_2T_{e3}$. In addition, the normalized gain value of approximately 2.74 × $10^{-4}$ $V^{-1}$ $cm^2$ achieved using this field-effect transistor (FET) device is several orders higher than those of the other 2D single crystal-based FET devices. Our results suggest that the $Si_2Te_3$ single crystal could be a benchmark candidate for the integration of prospective p–n junction circuits and photo-sensing applications.

Received 8th May 2021,
Accepted 15th July 2021

DOI: 10.1039/d1tc02129j

rsc.li/materials-c



## 1. Introduction

Since the discovery of graphene, two-dimensional (2D) materials have received a tremendous amount of interest owing to their exceptional physical properties, such as the distinct electronic structure, high electrical mobility, high thermal conductivity, large surface area, mechanical stiffness, and transparency.[1,2] In the bulk form, these materials are layer-by-layer stacked through weak van der Waals interactions and strong covalent bonding. By applying an external mechanical force, the weakly interacting layers can be easily peeled giving mono-layered to few-layered thicknesses.[3,4] Although graphene exhibits unique transport properties,[5,6] the zero bandgap nature leads to limitations in the optoelectronic properties,[7,8] there are plenty of 2D materials with suitable bandgaps that can be explored for optoelectronic applications. Among these, transition metal dichalcogenides (TMDs) show characteristic transport properties like those of graphene.[9–12] In addition, these materials exhibit unique electronic structures that span metals to semiconductors for potential uses in optoelectronic applications, particularly in photodetectors, solar cells, light-emitting diodes, and random lasers.[13–16] However, TMD-based materials lack natural p-type behavior, and hence the possibility of forming a p–n junction using 2D crystals is restricted in confined materials. The p–n intersection is an essential building block for many functional devices, therefore it is necessary to explore novel p-type based 2D semiconducting materials.[17,18]

Among numerous 2D crystals, only a few materials, such as black phosphorous,[19] germanium sulfide,[20] and gallium selenide,[21] exhibit natural p-type behaviors. In a recent discovery, it was

[a] Department of Mechanical Engineering, Chung Yuan Christian University, Taoyuan-32023, Taiwan. E-mail: cylin@cycu.edu.tw
[b] Center for Condensed Matter Sciences, National Taiwan University, Taipei-10617, Taiwan
[c] Department of Photonics Engineering, Technical University of Denmark, Roskilde-4000, Denmark. E-mail: urajeshiitr@gmail.com
[d] Institute of Physics, Academia Sinica, Taipei-11529, Taiwan. E-mail: sankarraman@gate.sinica.edu.tw
[e] Aston Institute of Photonic Technologies, Aston University, Birmingham-B4 7ET, UK
[f] Schulich Faculty of Chemistry, Technion-Israel Institute of Technology, Haifa-32000, Israel

† Electronic supplementary information (ESI) available. See DOI: 10.1039/d1tc02129j

‡ These authors contributed equally.

observed that silicon telluride ($Si_2Te_3$) possesses p-type behavior. Moreover, $Si_2Te_3$ exhibits unique physical properties, such as both indirect (1.85 eV) and direct (2.2 eV) optical band gaps, a large defect density ($\sim 10^{17}$ $cm^{-3}$), and prominent photoluminescence between 640–850 nm with a high quantum yield.[22,23] It is well known that silicon resulted in an extraordinary revolution in semiconductor technology owing to its dominant properties. Furthermore, Si offers a strong base for many classes of materials with outstanding performances, thus, it acts as a strong backbone in modern technologies.[24,25] These properties have inspired us to investigate the electronic and optoelectronic properties of the silicon-chalcogenide material $Si_2Te3$, for use in applications such as transistors and photodetectors. The phototransistor performance of the high-quality $Si_2Te_3$ single crystal has not been reported to date, to the best of our knowledge.

Phototransistor devices are used to transform light signals into electrical signals, they are a fundamental component in the modern miniaturized electronic industry. These devices are essential to the capture, identification, and visualization of optical signals.[26–28] They can be used to detect light of various sub-bands, such as ultraviolet, visible, and infrared rays with diverse applications in daily life, industrial, military, and agricultural applications. Ultraviolet detection can be used for monitoring the environment, and in the space and defense sectors, whereas visible light detection is used in video imaging, displays, optoelectronic storage, and industrial safety. Infrared detection applications are focused on night vision, remote control, and satellite remote sensing. Based on the 2D semiconducting materials, several photodetection devices have been explored to detect a wide spectral range of light from ultraviolet to infrared wavelengths. However, these devices suffer from severe drawbacks, such as instability, poor photoresponse, low on/off ratios, structural disorders, and defects. Therefore, there is an increasing demand to construct photo devices based on novel materials that are needed to enable high-performance-based photodetection to improve the functionality and commercialization of photodetectors.

There are few reports on the synthesis of 2D $Si_2Te_3$ materials in nanoplates and nanoribbons in a range of thicknesses from 50 to 1000 nm and a length of approximately 10 μm using standard vapor–liquid–solid (VLS) methods.[22,23,29] Most of these methods for the growth of 2D $Si_2Te_3$ often lead to the formation of impurity phases, such as Te and $SiTe_2$, owing to the high vapor pressure of the chalcogenides, which in turn cause large structural imperfections in the crystal lattices. It has been widely proved that the chemical vapor transport (CVT) technique can be used to grow high vapor pressure compounds because it facilitates a thermodynamically favored vapor phase reaction in the presence of an appropriate transporting agent. In this work, for the first time, we attempted to grow high-quality phase pure 2D $Si_2Te_3$ single crystals using the CVT method for the exfoliation of defect-free phase pure large area nanosheets. The high-quality few-layered nanosheets obtained from the exfoliation of CVT-grown $Si_2Te_3$ single crystals show excellent optoelectronic properties through the $Si_2Te_3$ field-effect transistor device (FET), in which the few-layered $Si_2Te_3$ nanosheets were used as a conducting channel. The carrier mobility of the

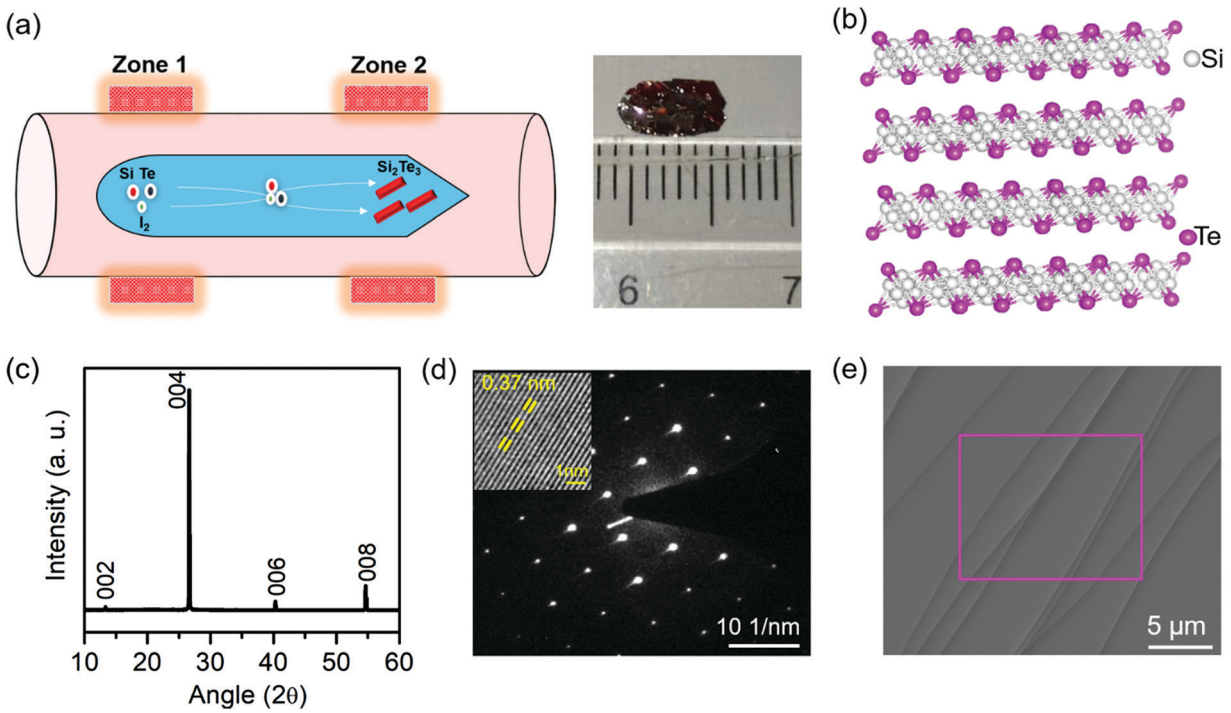


Fig. 1 (a) Schematic diagram of the CVT growth method with a photograph of the as-grown millimeter-sized $Si_2Te_3$ single crystal (on the right side). (b) Three-dimensional view of the crystal structure of $Si_2Te_3$. (c) XRD diffraction pattern of the $Si_2Te_3$ single-crystal revealing the preferred growth oriented along the *c*-axis. (d) Single crystallinity diffraction pattern of the $Si_2Te_3$ crystal, the inset shows the HR-TEM image with clear lattice fringes. (e) SEM image revealing the layered nature of the $Si_2Te_3$ single crystals.

exfoliated few-layered $Si_2Te_3$-FET was calculated and found to be approximately 1.03 $V^{-1}$ $cm^2$ $s^{-1}$ with p-type behavior and an on/off ratio of $10^3$. The few-layered $Si_2Te_3$ exhibits a high photoresponsivity of approximately 394 A $W^{-1}$ under the illumination of 6 nW at a 633 nm wavelength. The obtained photoresponsivity is higher compared with similar families of $Bi_2Te_3$ and $Sb_2Te_3$.

Moreover, the photo responsivity was enhanced further to 1396 A $W^{-1}$ by supplying a gate voltage at −40 V. In addition, the specific detectivity ($D^*$) and normalized gain were estimated and found to be approximatey 2.52 × $10^{12}$ Jones and 2.74 × $10^{-4}$ $V^{-1}$ $cm^2$, respectively. The obtained $D^*$ is almost equivalent to the commercial silicon photodiodes. The figures-of-merit obtained from the FET device demonstrate that few-layered $Si_2Te_3$ nanosheets are noteworthy potential candidates for device applications, mainly for the construction of phototransistors with a high photoresponse and multipurpose optoelectronics applications based on an amalgamation of p–n junctions.

## 2. Results and discussion

### 2.1. Crystal growth and characterization

Fig. 1a shows a schematic diagram of the CVT technique[30] used to grow high-quality bulk $Si_2Te_3$ single crystals. The crystal growth was carried out in a horizontal two-zone muffle furnace. The CVT reaction was conducted in a quartz ampoule of 100 cm and an outer/inner diameter of 12/10 cm. A stoichiometric quantity of the silicon and tellurium powders was ground and mixed well with the high vapor pressure transporting agent iodine. The precursor materials were loaded into the quartz ampoule and sealed at a pressure of approximately $10^{-5}$ torr. One end of the quartz tube containing the precursor material was kept in the hot furnace zone to maintain the temperature gradient. The reacting materials were heated to a high temperature of 900 °C, and the other end of the tube was maintained at a lower temperature of 850 °C. During the CVT growth process, the powder materials started to vaporize and react in the vapor state. They moved into the lower temperature area of the tube with a high vapor pressure transporting agent and finally deposited as bulk single-crystalline materials. After a growth period of 15 d, the shiny $Si_2Te_3$ single crystals were collected. The as-grown millimeter-sized $Si_2Te_3$ single crystals obtained using the CVT growth technique are shown on the right side of Fig. 1a.

The $Si_2Te_3$ single-crystal belongs to the trigonal crystal structure. Fig. 1b illustrates the architecture of $Si_2Te_3$, in which Si pairs are distributed among four equivalent orientations

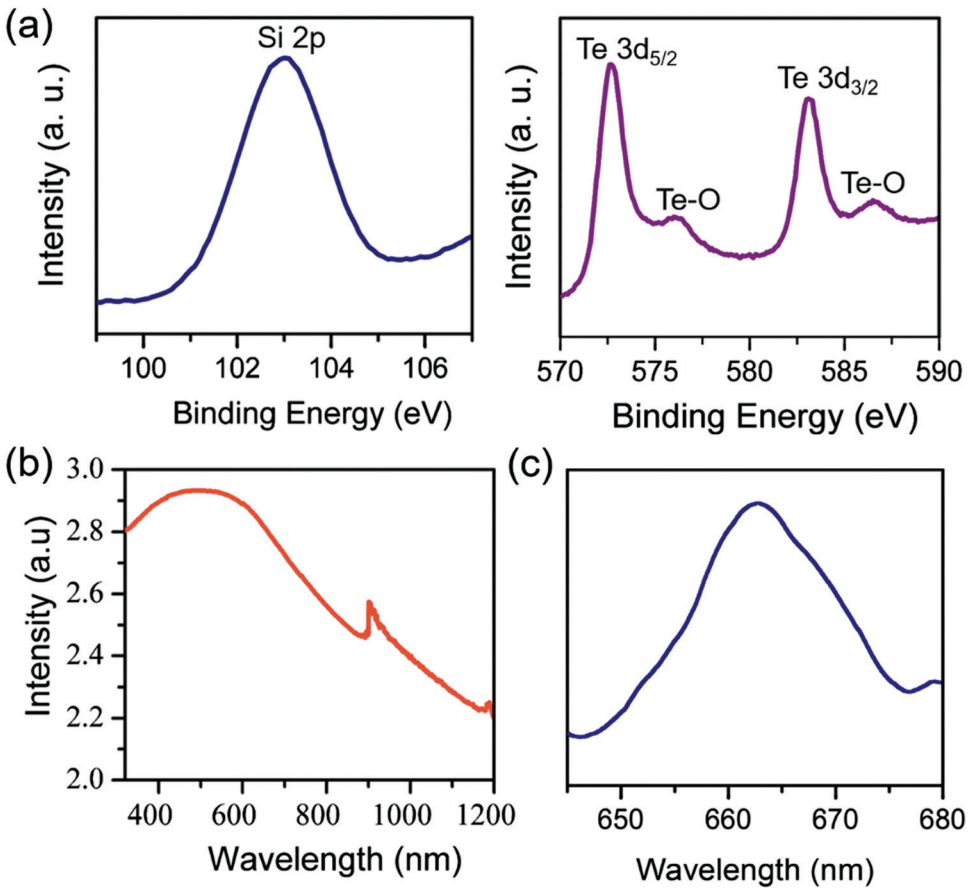


Fig. 2 (a) XPS spectra of the $Si_2Te_3$ crystal with binding energies of Si at 102.95 eV and Te at 572.5 and 582.9 eV, respectively. (b) Absorption spectrum of the as-grown $Si_2Te_3$ crystal. (c) Photoluminescence spectra of $Si_2Te_3$ showing an emission spectrum at 665 nm.

 

inside octahedral vacancies of a hexagonal close-packed Te lattice. The adjacent layers of these building blocks are bonded *via* weak van der Waals interactions, which in turn offer the best possibility for micromechanical exfoliation towards the monolayer or few-layered nanosheets of $Si_2Te_3$. The crystal structure and phase purity of the as-grown $Si_2Te_3$ single crystal were studied using X-ray diffraction (XRD) analysis. The observed XRD pattern for the $Si_2Te_3$ single-crystal (Fig. 1c) matches that of the trigonal crystal structure with the space group $P\bar{3}1c$ (JCPDF 00-022-1323). The complete absence of additional peaks corresponding to the secondary/impurity phase in the XRD pattern confirms the phase purity of the material. The repeated Miller planes corresponding to (00*l*) diffraction peaks reveal the single crystallinity and the preferred growth orientation along the *c*-axis. The single crystallinity of the as-grown $Si_2Te_3$ crystal was further confirmed using a selected area diffraction (SAED) pattern with bright diffraction spots, as shown in Fig. 1d. The inset shows the high-resolution transmission electron microscopy (HR-TEM) images, and the interplanar distance estimated from the HR-TEM image for the $Si_2Te_3$ single crystal is approximately 0.37 nm. The surface morphological and elemental distribution were identified using field emission-scanning electron microscopy (FE-SEM) and energy-dispersive-ray spectroscopy (EDAX). From the FE-SEM image, the stacking of the $Si_2Te_3$ layers in the 2D crystal was observed. The EDAX spectrum (Fig. S1 in the ESI†) and the elemental mapping (Fig. S2 in the ESI†) confirms the presence of silicon (Si) and telluride (Te) elements.

X-ray photoelectron spectroscopy (XPS) was also performed to examine the chemical state and elemental composition. Fig. 2a displays the typical XPS spectra of the as-grown $Si_2Te_3$ crystal,[31] in which three solid peaks were observed at binding energies around 102.95, 572. 5, and 582.9 eV. The peak at 102.95 eV corresponds to Si 2p, and the peaks at 572. 5 and 582.9 eV are linked to the binding energies of Te $3d_{5/2}$ and Te $3d_{3/2}$. The Te 3d shows a slight shift towards the lower binding energies by −0.5 eV compared to the pure Te at 573 eV owing to the chemical bonding between the Te and Si elements. The absorbance and photoluminescence were measured and are revealed in Fig. 2b and c. A solid spectral absorption on the bulk $Si_2Te_3$ crystal was observed from the near-infrared to the visible regions with a high absorption behavior, especially in the visible area, which shows that the $Si_2Te_3$ crystal is a strong photo absorbing material. Fig. 2c shows the photoluminescence spectrum and the wavelength of the emission maxima 665 nm correspond to a bandgap value of 1.86 eV, which agrees well with the reported bandgap of the bulk $Si_2Te_3$ compound.[29,32] The PL spectrum with an extended wavelength range from 500–900 nm reveals the defect emissions associated with the band edge emission and these are shown in Fig. S3 (ESI†).

### 2.2. Electronic and optoelectronic characterization

The electrical characteristics of the exfoliated few-layered $Si_2Te_3$ nanosheets were revealed by fabricating FET devices. Using the standard scotch tape process, the few-layered $Si_2Te_3$ nanosheets were transferred on a Si wafer and the top surface was covered by a dielectric $SiO_2$ layer with a thickness of 300 nm. The thickness of the exfoliated few-layered $Si_2Te_3$ nanosheet was found to be approximately 15 nm using atomic force microscopy (Fig. S4, ESI†). Then, Cr/Au (5/70 nm) electrodes were deposited at both ends of the $Si_2Te_3$ nanosheets using the typical lithographic procedure[33,34] as illustrated in Fig. 3a.

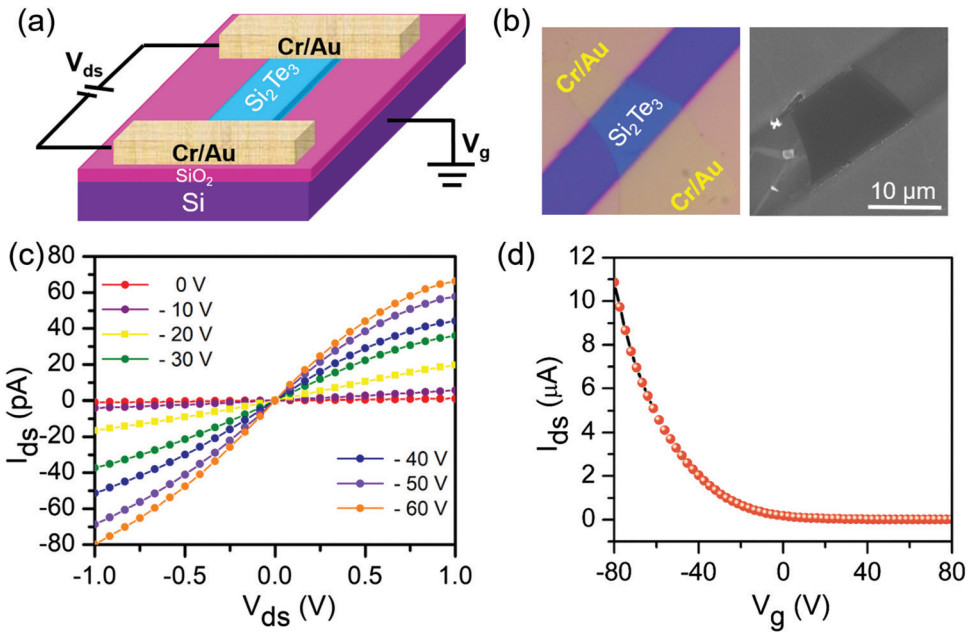


Fig. 3 Performances of the $Si_2Te_3$ transistor on a $SiO_2$/Si substrate. (a) The graphic structure of the $Si_2Te_3$-FET. (b) Optical and FE-SEM images of a few-layered $Si_2Te_3$-FET device. (c) Output characteristic curve of $Si_2Te_3$-FET with different gate voltages from 0 to −60 V at −10 V per step. (d) Transfer characteristics of $Si_2Te_3$-FET at 10 V of $V_{ds}$ and $V_g$ from −80 to +80 V.

Fig. 3b shows the optical and SEM images of the as-fabricated $Si_2Te_3$-FET device. The source-drain current *versus* the source-drain voltage ($I_{ds}$–$V_{ds}$) of the few-layered $Si_2Te_3$-FET (Fig. 3c) was measured at room temperature under ambient conditions with varying gate voltages ranging from 0 to −60 V. At a higher negative gate voltage ($V_g$), the $I_{ds}$–$V_{ds}$ curve increases gradually, revealing the $Si_2Te_3$ crystals have an apparent p-type behavior. The source-drain current *versus* back-gate voltage ($I_{ds}$–$V_g$) curve (Fig. 3d) measured at $V_{ds}$ = 10 V further confirms the p-type nature of the $Si_2Te_3$. The electron mobility ($\mu_e$) of the few-layered $Si_2Te_3$-FETwas calculated by the mobility equation of $\mu_e = L/W\,(\varepsilon_0\varepsilon_r/d)V_{ds}\,(dI_{ds}/dV_g)$, in which $L$ is the channel length, $W$ is the channel width, $\varepsilon_0$ is 8.85 × $10^{-12}$ $Fm^{-1}$, $\varepsilon_r$ is 3.9 for $SiO_2$, d is the thickness of $SiO_2$ (300 nm), $V_{ds}$ is the drain voltage 10 V, and $dI_{ds}/dV_g$ is the transconductance from the $I_{ds}$–$V_g$ curve.[35,36] From the equation, the calculated $\mu_e$ of our $Si_2Te_3$-FET device was observed to be approximately 1.03 $V^{-1}$ $cm^2$ $s^{-1}$, and the on/off ratio was about $10^3$ (Fig. S5, ESI†), which is comparable to other 2D materials. The presence of trap states between the $Si_2Te_3$ and the $SiO_2$ dielectric layer plays a prominent role in the charge carrier mobility. Reducing these trap states at the interface using a polymer coating enhances the mobility of the device.[37,38]

We further studied the $Si_2Te_3$-FET device performance for photocurrent generation using an illuminating laser with a wavelength of 633 nm at room temperature, the schematic illustration is shown in Fig. 4a. Photocurrent generation is an important figure of merit for good photo-detecting devices. The $I_{ds}$–$V_{ds}$ measurements in the dark and in the presence of various laser powers are presented in Fig. 4b. Upon laser illumination, the $I_{ds}$–$V_{ds}$ current increases dramatically compared to dark conditions owing to the outstanding photoresponse behavior of the $Si_2Te_3$ crystals. Furthermore, the photogenerated current progressively increased as the laser power intensities increased from 6 to 68 nW. Fig. 4b shows that the generated photocurrent ($I_{ph}$) was extracted by deducting the $I_{ds}$ obtained in the dark and light ($I_{ph} = I_{light} - I_{dark}$). The $I_{ph}$ *versus* incident power was plotted in Fig. 4c, in which the photocurrent rises sub-linearly following a power law of $I_{ph} \approx P^{0.95}$. Photoresponsivity ($R_\lambda$) is one of the essential qualities necessary for photo devices, and is defined as the photocurrent generated per unit power of incident light power and is expressed as $R_\lambda = \Delta I_\lambda/(P_\lambda S) = [[et\alpha/(h\nu)]\cdot(\tau_l/\tau_t)]$, in which $\Delta I_\lambda$ is the generated photocurrent, $P_\lambda$ is the incident light power, $S$ is the illuminated area, $\alpha$ is absorption coefficient, t is the thickness of the channel material at incident photon energy ($h\nu$), and $\tau_l/\tau_t$ is the ratio of the lifetime of minority carriers ($\tau_l$) to the transit time of the majority carriers ($\tau_t$).[39,40] From the above equation, the calculated $R_\lambda$ of $Si_2Te_3$-FET is estimated to be approximately 394 A $W^{-1}$ at 6 nW as a function of $V_{ds}$ = 10 V and $V_g$ = 0 V,

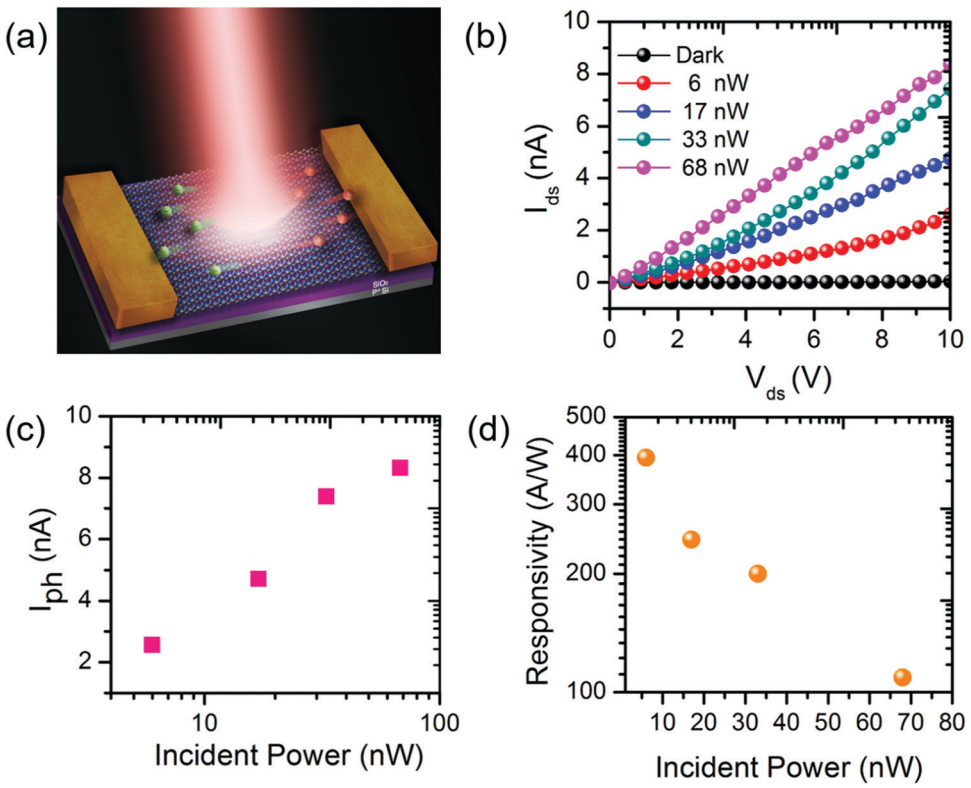


Fig. 4 Characteristics of $Si_2Te_3$ photodetection: (a) schematic illustration of a few-layered $Si_2Te_3$-FET device investigated using a 633 nm excitation laser. (b) The $I_{ds}$–$V_{ds}$ curve at different laser power intensities (6, 17, 33, and 68 nm). (c) Photocurrent ($I_{ph}$) plotted as a function of the incident laser power (P) measured at $V_{ds}$ = 10 V and $V_g$ = 0 V. (d) Photo responsivity of the few-layered $Si_2Te_3$ photodetector under various laser intensities at a wavelength of 633 nm.

 

which is greater than the recently reported $Si_2Te_3$[41] photodetector and the other compounds in the chalcogenides, such as $Bi_2Te_3$,[42] $Sb_2Te_3$,[43] and the other 2D crystals[44–46] (Table S1, ESI†). This high $R_\lambda$ for $Si_2Te_3$-FET can be attributed to the exceptional absorption nature of $Si_2Te_3$ in an extensive spectrum range from the near-infrared to the visible region, along with the fast and productive separation of photocarriers in the spatial 2D crystals of the $Si_2Te_3$ nanosheets with delayed recombination of the electron–hole, thus allowing a highly proficient photoresponsive conversion.[47]

Furthermore, the $R_\lambda$ was significantly improved by applying the back gate voltage. Fig. 5a depicts the $I_{ds}$ curve of $Si_2Te_3$-FET as a function of various gate voltage ranges from −40 V to 40 V under dark and illuminated conditions. At a wavelength of 633 nm and illumination value of 2 μW, the current at −40 V is almost 2.5 times larger than that in the dark, and the corresponding $I_{ph}$ *versus* $V_g$ curve is displayed in Fig. S6 of the ESI.† From the photo curve, the $R_\lambda$ was further estimated under different $V_g$ values (−40 V to 40 V); it reached the maximum responsivity of approximately 1396 A $W^{-1}$ at 10 V of $V_{ds}$ and −40 V of $V_g$ (Fig. 5b). The mechanism behind this high value of $R_\lambda$ is illustrated in Fig. 5c. Firstly, the $I_{ds}$ remains higher when the $V_g$ is greater than the threshold voltage ($V_{th}$) owing to the Fermi level band shifting upwards. The high measured current under illumination (laser On) generates more electron–hole pairs for the valence-to-conduction band transition. Excessive electrons and holes can be swept towards the source-drain electrodes *via* the electric field in the channel; this results in a significant photocurrent enhancement. Secondly, the $I_{ds}$ remains low when the $V_g$ is less than the threshold voltage ($V_{th}$), owing to the downward shift of the Fermi level band.[48] When the laser is switched Off, the $I_{ds}$ is much smaller than when the laser is On owing to the reduced carrier electron and hole pairs being swept between the electrode and the conducting channel during electric field supply. We have also measured the wavelength dependence on responsivity by varying the wavelengths from 900 to 400 nm at a power intensity of approximately 60 nW, $V_{ds}$ = 10 V, and $V_g$ = −40 V. The responsivity was found to increase with the increasing wavelength (Fig. S7 in the ESI†), which is well consistent with the optical absorption results of $Si_2Te_3$.

Finally, the critical parameters of photodetection, such as the specific detectivity, normalized gain, and response time, were projected. Specific detectivity is typically estimated using the formula $D^* = (S{\cdot}\Delta f)^{1/2}/\mathrm{NEP}$, in which $S$ and $\Delta f$ are the active area of the photodetector and the electrical bandwidth, respectively, and NEP denotes the noise equivalent power. The NEP signifies the minimum optical power at which a photodetector can distinguish a signal from noise. The above equation can be represented as $D^* = R_\lambda\, S^{1/2}/(2eI_{dark})^{1/2}$, in which $R_\lambda$, $S$, $e$, and

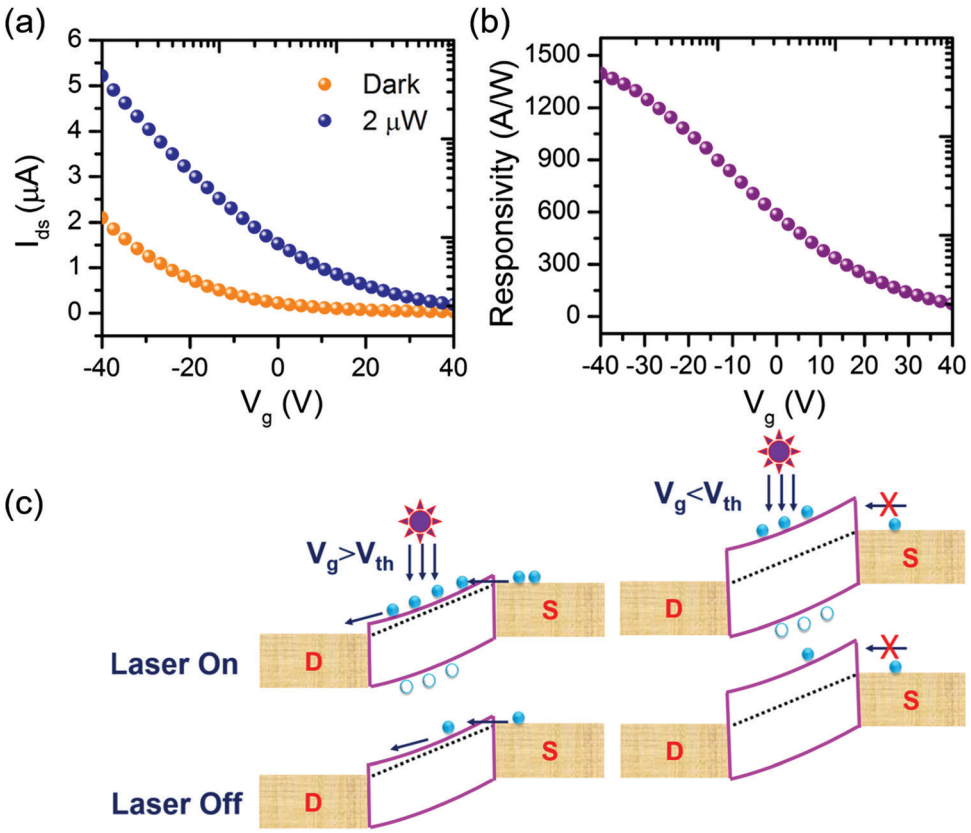


Fig. 5 (a) The transfer curve of the few-layered $Si_2Te_3$ under illuminated and dark states. (b) Photo responsivity of the fe-layered $Si_2Te_3$ photodetector under various $V_g$ from −0 to +40 V at $V_{ds}$ = 10 V. (c) Energy band diagram at the greatest and lowest threshold voltages in the presence and absence of light illumination.

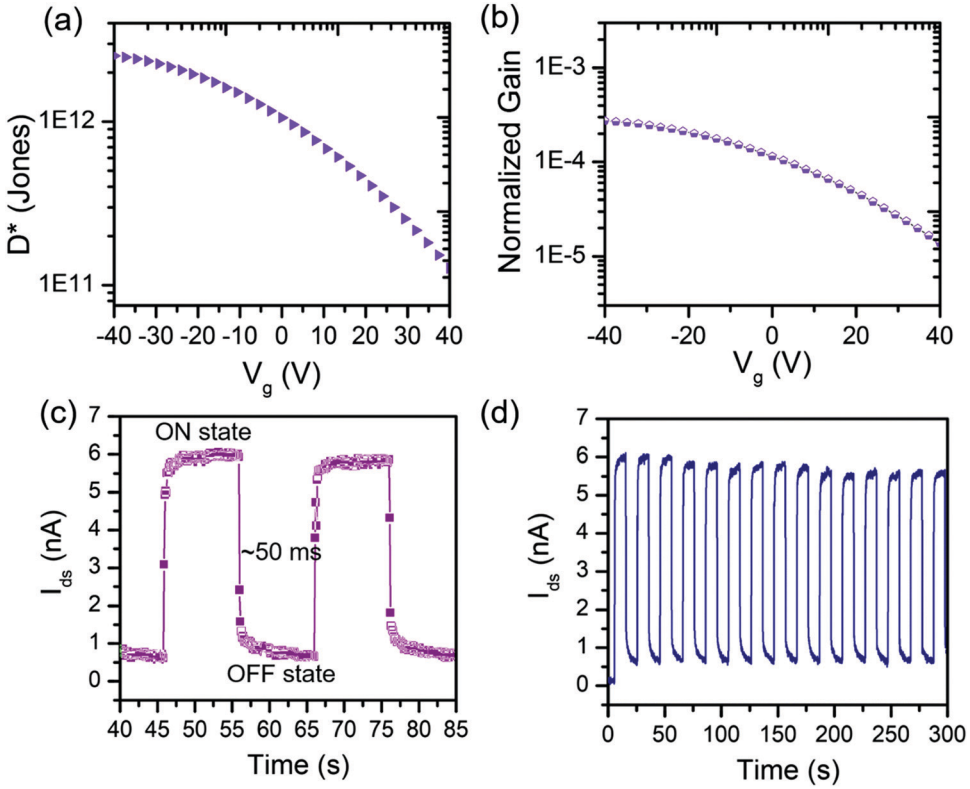


Fig. 6 (a) $D^*$ of the few-layered $Si_2Te_3$ photodetector was investigated as a function of the excitation wavelength at $P$ = 2 μW, $V_g$ = 0 V, and $V_{ds}$ = 10 V. (b) The normalized gain of $Si_2Te_3$ was estimated as 2.74 × $10^{-4}$ $V^{-1}$ $cm^2$. Time-resolved photoresponse of the $Si_2Te_3$ photodetector (c). The single ON–OFF cycle of illumination at $\lambda$ = 633 nm and the rising time, estimated as 50 ms. (d) The photoswitching stability of the $Si_2Te_3$ photodetector in response to a train of continuous ON–OFF illumination.

$I_{dark}$ are the photoresponsivity at a lower NEP value, effective area, elementary charge, and dark current, respectively.[49,50] Based on the above equation, the calculated $D^*$ is approximately 2.52 × $10^{12}$ Jones at $V_g$ = −40 V and $V_{ds}$ = 10 V (Fig. 6a), which are better than and similar to, respectively, the recently reported 2D materials[51–53] (Table S1, ESI†) and almost equal to commercial Si[54] and InGaAs photodetectors.[55] The normalized gain ($\Gamma_n$) is obtained from the products of $\eta$, $\tau$, and $\mu$ and is written as $\Gamma_n = \eta\tau\mu$, in which $\eta$ is the quantum efficiency, $\tau$ is the carrier lifetime, and $\mu$ is the carrier mobility.[56] The gain ($\Gamma$) is defined as the number of photocarriers in circulation between the electrodes before it recombines. Hence, it is denoted as the ratio of the carrier lifetime to the transit time ($\tau_t$) and is written as:[56]

$$\Gamma = \tau/\tau_t = \tau\mu V/l^2 \quad (1)$$

In which, $V$ is the bias voltage, and $L$ is the channel length of the device. $\Gamma$ has a linear relationship with $R_\lambda$ and $I_{ph}$, therefore the $\Gamma$ can also be estimated using:

$$\Gamma = (E/e)\,(R/\eta) = E/e\,(I_{ph}/p\eta) \quad (2)$$

In which, $E$ is the photon energy, and e is the elementary charge, using eqn (1) and (2), the $\Gamma_n$ can be rewritten as $\Gamma_n = (E/e)\,(I_{ph}/p)\,(l^2/V)$, from this relationship, the calculated value of $\Gamma_n$ can be obtained as 2.74 × $10^{-4}$ $V^{-1}$ $cm^2$ (Fig. 6b). This value is two orders higher than the monolayer $MoS_2$[13] and UCNP-graphene photodetectors[57] (Table S1, ESI†). The real-time measurements ($I_{ds}$–$t$) were performed to evaluate the response speed and the switching stability of the $Si_2Te_3$-FET. The $I_{ds}$–$t$ curve was recorded by illuminating the $Si_2Te_3$ device with a 633 nm wavelength. Fig. 6c shows the rapid rise in the current when the light is switched ON and the sudden drop when the light is turned OFF. From this $I_{ds}$–$t$ curve, the response speed of $Si_2Te_3$-FET was found to be approximately 50 ms. The ON–OFF illumination was performed continuously for 300 s (Fig. 6d). The reproducible ON–OFF curve and long-term stability without any degradation during long lasting laser illumination confirm our $Si_2Te_3$ photodetector device is robust.

## 3. Conclusions

A silicon-based chalcogenide class of two-dimensional p-type $Si_2Te_3$ single crystals has been successfully grown using the CVT method using iodine as a transporting agent. The $Si_2Te_3$ single-crystal reveals the good crystallinity and phase purity and promises excellent optoelectronic properties. The FET device fabricated with few-layered $Si_2Te_3$ nanosheets obtained using mechanical exfoliation showed an outstanding performance, with a high photoresponsivity (∼1396 A $W^{-1}$), large specific

 

detectivity ($\sim 2.52 \times 10^{12}$ Jones), and a high order of normalized gain ($2.74 \times 10^{-4}$ $V^{-1}$ $cm^2$). These values are relatively more prominent compared to other 2D single crystals-based FET devices. The p-type semiconducting nature with the exceptional photoresponse of the $Si_2Te_3$ single crystals could significantly impact the field of optoelectronics and play a vital role in the integration of p–n junction-based devices for light detection applications.

# 4. Experimental section

### 4.1. Mechanical exfoliation and device fabrication

The as-grown $Si_2Te_3$ single crystal was exfoliated into few-layered nanosheets using the standard Scotch tape exfoliation process. The exfoliated nanoflakes were moved onto the silicon substrate and coated with a 300 nm thick silicon dioxide dielectric layer. A thin TEM grid was used to construct the source/drain (S/D) electrodes on the edges of the transferred nanosheets. Then, 70 nm of gold (Au) with a 5 nm bonding layer of chromium was deposited using a thermal evaporator under $10^{-6}$ Torr vacuum conditions. After device fabrication, post-annealing at 200 °C in a nitrogen atmosphere was carried out for 1 h.

### 4.2. Characterizations

XRD analyses were carried out using a Bruker D2 PHASER (CuKα radiation). Scanning electron microscopy (SEM) (FEI, Nova 200) and transmission electron microscopy (TEM) (JEOL, JEM-2100F) were used to examine the morphology and crystallinity of the $Si_2Te_3$ single crystal. A V-770 UV-Visible/NIR spectrophotometer was used to measure the absorption spectrum of the $Si_2Te_3$ single crystals. The $I_{ds}$–$V_{ds}$ curves were measured using a source meter (Keithley, 2636A), with an optical system including a He–Ne laser, power meter (Ophir, Nova II), and bandpass filters.

# Conflicts of interest

There are no conflicts to declare.

# Acknowledgements

This work was supported by the Ministry of Science and Technology (MOST), Taiwan, under grant numbers MOST-110-2221-E-033-022-, MOST-109-2222-E-003-001-MY2 and MOST-110-2112-M-001-065-MY3. Academia Sinica funded i-MATE financial support AS-iMATE-109-13. RCM and AR want to thank the Marie Skłodowska-Curie Individual Fellowship (MOFUS, # 795356).

# References

1 T. Chowdhury, E. C. Sadler and T. J. Kempa, *Chem. Rev.*, 2020, **120**, 12563.
2 S. Stankovich, D. A. Dikin, G. H. B. Dommett, K. M. Kohlhaas, E. J. Zimney, E. A. Stach, R. D. Piner, S. T. Nguyen and R. S. Ruoff, *Nature*, 2006, **442**, 282.
3 Y. Huang, Y. H. Pan, R. Yang, L.-H. Bao, L. Meng, H.-L. Luo, Y.-Q. Cai, G.-D. Liu, W.-J. Zhao, Z. Zhou, L.-M. Wu, Z.-L. Zhu, M. Huang, L.-W. Liu, L. Liu, P. Cheng, K.-H. Wu, S.-B. Tian, C.-Z. Gu, Y.-G. Shi, Y.-F. Guo, Z. G. Cheng, J.-P. Hu, L. Zhao, G.-H. Yang, E. Sutter, P. Sutter, Y.-L. Wang, W. Ji, X.-J. Zhou and H.-J. Gao, *Nat. Commun.*, 2020, **11**, 2453.
4 M. Yi and Z. Shen, *J. Mater. Chem. A*, 2015, **3**, 11700.
5 A. K. Geim, *Science*, 2009, **324**, 530.
6 K. S. Novoselov, V. I. Falko, L. Colombo, P. R. Gellert, M. G. Schwab and K. Kim, *Nature*, 2012, **490**, 192.
7 K. F. Mak and J. Shan, *Nat. Photonics*, 2016, **10**, 216.
8 I. Meric, M. Y. Han, A. F. Young, B. Ozyilmaz, P. Kim and K. L. Shepard, *Nat. Nanotechnol.*, 2008, **3**, 654.
9 B. Radisavljevic, A. Radenovic, J. Brivio, V. Giacometti and A. Kis, *Nat. Nanotechnol.*, 2011, **6**, 147.
10 Y. Shi, C. Hua, B. Li, X. Fang, C. Yao, Y. Zhang, Y.-S. Hu, Z. Wang, L. Chen, D. Zhao and G. D. Stucky, *Adv. Funct. Mater.*, 2013, **23**, 1832.
11 D. Ovchinnikov, A. Allain, Y.-S. Huang, D. Dumcenco and A. Kis, *ACS Nano*, 2014, **8**, 8174.
12 Y.-F. Lin, Y. Xu, S.-T. Wang, S.-L. Li, M. Yamamoto, A. A.-Ferreira, W. Li, H. Sun, S. Nakaharai, W.-B. Jian, K. Ueno and K. Tsukagoshi, *Adv. Mater.*, 2014, **26**, 3263.
13 O. L.-Sanchez, D. Lembke, M. Kayci, A. Radenovic and A. Kis, *Nat. Nanotechnol.*, 2013, **8**, 497.
14 R. K. Ulaganathan, K. Yadav, R. Sankar, F.-C. Chou and Y.-T. Chen, *Adv. Mater. Interfaces*, 2019, **6**, 1801336.
15 J. Wang, Y. J. Zhou, D. Xiang, S. J. Ng, K. Watanabe, T. Taniguchi and G. Eda, *Adv. Mater.*, 2020, **32**, 2001890.
16 T. Dixit, A. Arora, A. Krishnan, K. L. Ganapathi, P. K. Nayak and M. S. R. Rao, *ACS Omega*, 2018, **3**, 14097.
17 J. Ahn, P. J. Jeon, S. R. A. Raza, A. Pezeshki, S.-W. Min, D. K. Hwang and S. Im, *2D Mater.*, 2016, **3**, 045011.
18 W. Hu and J. L. Yang, *J. Mater. Chem. C*, 2017, **5**, 12289.
19 S. Kim, G. Myeong, W. Shin, H. Lim, B. Kim, T. Jin, S. Chang, K. Watanabe, T. Taniguchi and S. Cho, *Nat. Nanotechnol.*, 2020, **15**, 203.
20 R. K. Ulaganathan, Y.-Y. Lu, C.-J. Kuo, S. R. Tamalampudi, R. Sankar, K. M. Boopathi, A. Anand, K. Yadav, R. J. Mathew, C.-R. Liu, F.-C. Chou and Y.-T. Chen, *Nanoscale*, 2016, **8**, 2284.
21 D. J. Late, B. Liu, J. Luo, A. Yan, H. S. S. R. Matte, M. Grayson, C. N. R. Rao and V. P. Dravid, *Adv. Mater.*, 2012, **24**, 3549.
22 M. Wang, G. Lahti, D. Williams and K. J. Koskki, *ACS Nano*, 2018, **12**, 6163.
23 S. Keuleyan, M. Wang, F. R. Chung, J. Commons and K. J. Koski, *Nano Lett.*, 2015, **15**, 2285.
24 C. Battaglia, A. Cuevas and S. D. Wolf, *Energy Environ. Sci.*, 2016, **9**, 1552.
25 J. Schwan, G. Nava and L. Mangolini, *Nanoscale Adv.*, 2020, **2**, 4368.
26 Y. Zou, Y. Zhang, Y. Hu and H. Gu, *Sensors*, 2018, **18**, 2072.

27 W. Yang, K. Hu, F. Teng, J. Weng, Y. Zhang and X. Fang, *Nano Lett.*, 2018, **18**, 4697.
28 M. Long, Y. Wang, P. Wang, X. Zhou, H. Xia, C. Luo, S. Huang, G. Zhang, H. Yan, Z. Fan, X. Wu, X. Chen, W. Lu and W. Hu, *ACS Nano*, 2019, **13**, 2511.
29 J. Kwak, K. Thiyagarajan, A. Giri and U. Jeong, *J. Mater. Chem. C*, 2019, **7**, 10561.
30 R. K. Ulaganathan, R. Sankar, C.-Y. Lin, R. C. Murugesan, K. Tang and F.-C. Chou, *Adv. Electron. Mater.*, 2019, **6**, 900794.
31 K. Wu, W. Sun, Y. Jiang, J. Chen, L. Li, C. Cao, S. Shi, X. Shen and J. Cui, *J. Appl. Phys.*, 2017, **122**, 075701.
32 X. Song, Y. Ke, X. Chen, J. Liu, Q. Hao, D. Wei and W. Zhang, *Nanoscale*, 2020, **12**, 11242.
33 S. R. Tamalampudi, Y.-Y. Lu, R. K. Ulaganathan, R. Sankar, C.-D. Liao, K. M. Boopathi, C.-H. Cheng, F.-C. Chou and Y.-T. Chen, *Nano Lett.*, 2014, **14**, 2800.
34 P. Perumal, R. K. Ulaganathan, R. Sankar, Y.-M. Liao, T.-M. Sun, M.-W. Chu, F.-C. Chou, Y.-T. Chen, M.-H. Shih and Y.-F. Chen, *Adv. Funct. Mater.*, 2016, **26**, 3630.
35 S. Sucharitakul, N. J. Goble, U. R. Kumar, R. Sankar, Z. A. Bogorad, F.-C. Chou, Y.-T. Chen and X. P. A. Gao, *Nano Lett.*, 2015, **15**, 3815.
36 C. R. P. Inbaraj, V. K. Gudelli, R. J. Mathew, R. K. Ulaganathan, R. Sankar, H. Y. Lin, H.-I. Lin, Y.-M. Liao, H.-Y. Cheng, K.-H. Lin, F.-C. Chou, Y.-T. Chen, C.-H. Lee, G.-Y. Guo and Y.-F. Chen, *ACS Appl. Mater. Interfaces*, 2019, **11**, 24269.
37 P.-H. Ho, Y.-R. Chang, Y.-C. Chu, M.-K. Li, C.-A. Tsai, W.-H. Wang, C.-H. Ho, C.-W. Chen and P.-W. Chiu, *ACS Nano*, 2017, **11**, 7362.
38 W. Feng, W. Zheng, W. Cao and P. Hu, *Adv. Mater.*, 2014, **26**, 6587.
39 D. Wu, Y. Wang, L. Zeng, C. Jia, E. Wu, T. Xu, Z. Shi, Y. Tian, X. Li and Y. H. Tsang, *ACS Photonics*, 2018, **5**, 3820.
40 P. Perumal, R. K. Ulaganathan, R. Sankar and L. Zhu, *Appl. Surf. Sci.*, 2021, **535**, 147480.
41 J. W. Chen, C. Y. Tan, G. Li, L. J. Chen, H. L. Zhang, S. Q. Yin, M. Li, L. Li and G. H. Li, *Small*, 2021, **17**, 2006496.
42 J. L. Liu, H. Wang, X. Li, H. Chen, Z. K. Zhang, W. W. Pan, G. Q. Luo, C. L. Yuan, Y. L. Ren and W. Lei, *J. Alloys Compd.*, 2019, **798**, 656.
43 K. Zheng, L.-B. Luo, T.-F. Zhang, Y.-H. Liu, Y.-Q. Yu, R. Lu, H.-L. Qiu, Z.-J. Li and J. C. A. Huang, *J. Mater. Chem. C*, 2015, **3**, 9154.
44 C. Zhou, S. Zhang, Z. Lv, Z. Ma, C. Yu, Z. Feng and M. Chan, *npj 2D Mater. Appl.*, 2020, **4**, 46.
45 W. W. Tang, C. Liu, L. Wang, X. Chen, M. Luo, W. Guo, S.-W. Wang and W. Lu, *Appl. Phys. Lett.*, 2017, **11**, 53502.
46 E. Zhang, Y. Jin, X. Yuan, W. Wang, C. Zhang, L. Tang, S. Liu, P. Zhou, W. Hu and F. Xiu, *Adv. Funct. Mater.*, 2015, **25**, 4076.
47 K. Ziegler and U. Birkholz, *Phys. Status Solidi A*, 1977, **39**, 467.
48 C. R. P. Inbaraj, R. J. Mathew, G. Haider, T.-P. Chen, R. K. Ulaganathan, R. Sankar, K. P. Bera, Y.-M. Liao, M. Kataria, H.-I. Lin, F.-C. Chou, Y.-T. Chen, C.-H. Lee and Y.-F. Chen, *Nanoscale*, 2018, **10**, 18642.
49 M. Buscema, J. O. Island, D. J. Groenendijk, S. I. Blanter, G. A. Steele, H. S. J. van der Zant and A. C. Gomez, *Chem. Soc. Rev.*, 2015, **44**, 3691.
50 G. Su, V. G. Hadjiev, P. E. Loya, J. Zhang, S. Lei, S. Maharjan, P. Dong, P. M. Ajayan, J. Lou and H. Peng, *Nano Lett.*, 2015, **15**, 506.
51 W. Wang, X. Zeng, J. H. Warner, Z. Guo, Y. Hu, Y. Zeng, J. Lu, W. Jin, S. Wang, J. Lu, Y. Zeng and Y. Xiao, *ACS Appl. Mater. Interfaces*, 2020, **12**, 33325.
52 M. Long, A. Gao, P. Wang, H. Xia, C. Ott, C. Pan, Y. Fu, E. Liu, X. Chen, W. Lu, T. Nilges, J. Xu, X. Wang, W. Hu and F. Miao, *Sci. Adv.*, 2017, **3**, e1700589.
53 M. Dai, H. Chen, R. Feng, Y. Hu, H. Yang, G. Liu, X. Chen, J. Zhang, C.-Y. Xu and P. A. Hu, *ACS Nano*, 2018, **12**, 8739.
54 X. Gong, M. Tong, Y. Xia, W. Cai, J. S. Moon, Y. Cao, G. Yu, C.-L. Shieh, B. Nilsson and A. J. Heeger, *Science*, 2009, **325**, 1665.
55 J. Kaniewski and J. Piotrowski, *Opto-Electron. Rev.*, 2004, **12**, 139.
56 S. Ghosh, W. C. Chiang, M. Y. Fakhri, C. T. Wu, R. S. Chen and S. Chattopadhyay, *Nano Energy*, 2020, **67**, 104258.
57 M. K. Thakur, A. Gupta, M. Y. Fakhri, R. S. Chen, C. T. Wu, K. H. Lin and S. Chattopadhyay, *Nanoscale*, 2019, **11**, 9716.

 